

# Learning Chern Numbers of Topological Insulators with Gauge Equivariant Neural Networks

Longde Huang <sup>a1</sup>, Oleksandr Balabanov<sup>2</sup>, Hampus Linander<sup>1,4</sup>, Mats Granath<sup>3</sup>, Daniel Persson<sup>1</sup>,  
Jan E. Gerken <sup>b1</sup>

<sup>1</sup>Department of Mathematical Sciences, Chalmers University of Technology and University of Gothenburg,  
SE-412 96 Gothenburg, Sweden.

<sup>2</sup>Department of Physics, Stockholm University, AlbaNova University Center, SE-106 91 Stockholm, Sweden

<sup>3</sup>Department of Physics, University of Gothenburg, SE-412 96 Gothenburg, Sweden

<sup>4</sup>VERSES AI Research Lab, Los Angeles, USA

## Abstract

Equivariant network architectures are a well-established tool for predicting invariant or equivariant quantities. However, almost all learning problems considered in this context feature a global symmetry, i.e. each point of the underlying space is transformed with the same group element, as opposed to a local “gauge” symmetry, where each point is transformed with a different group element, exponentially enlarging the size of the symmetry group. Gauge equivariant networks have so far mainly been applied to problems in quantum chromodynamics. Here, we introduce a novel application domain for gauge-equivariant networks in the theory of topological condensed matter physics. We use gauge equivariant networks to predict topological invariants (Chern numbers) of multiband topological insulators. The gauge symmetry of the network guarantees that the predicted quantity is a topological invariant. We introduce a novel gauge equivariant normalization layer to stabilize the training and prove a universal approximation theorem for our setup. We train on samples with trivial Chern number only but show that our models generalize to samples with non-trivial Chern number. We provide various ablations of our setup. Our code is available at <https://github.com/sitronsea/GENet/tree/main>.

tures [1]. This approach has been successfully applied in a variety of domains, from medical imaging [2] to high-energy physics [3] and quantum chemistry [4]. As we show in this paper, this perspective is particularly valuable for studying topological insulators, a class of materials which has been one of the main areas of interest in condensed matter physics over the last two decades [5, 6], with a broad range of applications, including spintronics and magneto-electronics [7], photonics [8], quantum devices [9], and quantum computing [10, 11, 12].

The mathematical field of topology studies objects which cannot be deformed continuously into each other. For instance, a doughnut is topologically equivalent to a coffee cup (the hole in the doughnut becoming the hole in the handle) but not to a ball (which does not have a hole). Topological insulators are materials whose interior is insulating yet whose surface or boundary supports robust conduction. This behavior arises from the different topologies of the electronic band structures inside and outside of the material. The topologies are characterized by quantities which do not change under continuous deformations respecting the underlying system’s physical symmetries; these are known as topological invariants.

In the context of topological insulators, the deformations we are interested in only affect the phase of the electron wavefunction and therefore leave the underlying physical system unchanged, corresponding to a so-called gauge symmetry. Even though these phase changes are locally unphysical, they accumu-

## 1 Introduction

Geometric deep learning is a subfield of machine learning that takes advantage of the geometric and topological structures inherent in complex data to construct more efficient neural network architec-

<sup>a</sup>longde@chalmers.se

<sup>b</sup>gerken@chalmers.se

late over momentum space into the *Chern number*. This is a physically relevant topological invariant and the learning target of the models studied here. We construct a neural network which predicts the Chern number given a specific discretized version of the wave function as detailed below. In particular, our focus will be on so-called multi-band topological insulators in which several wave functions are combined into a vector. Previous works could construct deep learning systems which predict Chern numbers for materials with only 1 filled band [13, 14]. Perhaps surprisingly, these models fail to learn Chern numbers for higher-band systems, pointing to a fundamental challenge in the multi-band regime. In contrast, our model is able to predict Chern numbers of materials with at least 7 filled bands.

We stress that learning the Chern number may be viewed as a toy model for more interesting topological insulators. However, since even learning the Chern number is challenging, this is a stepping stone towards more sophisticated physical systems exhibiting richer topological—and consequently physical—properties.

We identify the *gauge symmetry* of the system as the central reason for the failure of traditional approaches in the high-band setting and instead propose to use a gauge equivariant network for learning topological invariants such as the Chern number. Usual group equivariant networks  $\mathcal{N} : X \rightarrow Y$  satisfy the constraint  $\mathcal{N}(\rho_X(g)x) = \rho_Y(g)\mathcal{N}(x) \forall g \in G$  with symmetry group  $G$  and representations  $\rho_{X,Y}$  on the input- and output spaces, respectively. In contrast, a gauge equivariant network satisfies a much stronger condition in which the group element  $g$  can depend on the input  $x$ :  $\mathcal{N}(\rho_X(g_x)x) = \rho_Y(g_x)\mathcal{N}(x)$ . In our case, the input space  $X$  is the Fourier transform of the position, the so-called *Brillouin zone* of the material, and  $G = \text{U}(N)$  for a system with  $N$  filled bands.

In a discretized input domain  $X$  in  $d$  dimensions with  $p$  points per dimension, a gauge symmetry effectively means that the total symmetry group of the problem consists of  $p^d$  copies of  $G$ . This enormous enlargement of the symmetry group explains why non-equivariant networks are often unable to learn tasks which feature a gauge symmetry. We therefore claim that gauge-equivariant networks are necessary to learn high-band Chern numbers of topological insulators. This is a novel application for gauge equivariant neural networks, which thus far have mainly found applications within the realm of lattice gauge

theories for quantum chromodynamics. In particular, we cast the problem at hand in a form in which we can use an adapted version of the Lattice Gauge Equivariant Convolutional Neural Networks (LGE-CNNs) [15] to learn multiband Chern numbers.

Our main contributions are as follows:

- We provide a novel application of  $\text{U}(N)$ -gauge equivariant neural networks to the task of learning higher-band Chern numbers. The resulting model can predict Chern numbers in two dimensions for systems with at least  $N = 7$  filled bands. In contrast, previous models could only handle the trivial case of a  $\text{U}(1)$ -symmetry.
- Our model is also the first to be able to learn higher-dimensional ( $D = 4$ ) Chern numbers of multi-band topological insulators.
- We prove a universal approximation theorem for our architecture in this context which shows that our model can approximate all  $\text{U}(N)$  gauge invariants arbitrarily well. We perform ablations over different gauge equivariant architectures motivated by this theoretical investigation.
- To stabilize the training, we introduce a new gauge equivariant normalization layer. By training our purely local network with a novel combinations of loss functions, we obtain a model which generalizes from trivial to non-trivial Chern numbers and to unseen lattice sizes.

## 2 Literature Review

Gauge equivariant networks have been considered in two different settings. In the first setting, the gauge symmetry concerns local coordinate changes in the domain of the feature maps [16, 17, 1]. This case was first studied theoretically in [18] and models respecting this symmetry were introduced in [19, 20]. Applications of gauge equivariant networks to lattice quantum chromodynamics (QCD) fall into the second setting, where the gauge transformations act on the co-domain of the feature maps. An important problem in lattice QCD is sampling configurations from the lattice action, a problem for which gauge equivariant normalizing flows [21, 22, 23, 24, 25] as well as gauge equivariant neural-network quantum

states [26] have been used. In contrast, our model is based on a gauge equivariant prediction model developed for lattice QCD [15].

Machine learning for quantum physics has seen an explosive development over the last decade with applications in condensed matter physics, materials science, quantum information and quantum computing to name a few [27, 28, 29, 30]. In this brief overview we focus on machine learning of topological states of matter. Early ground-breaking work in this area include [31] that used supervised learning on small convolutional neural networks for identifying the ground state of the Ising lattice gauge theory, as well as [32] that developed an unsupervised method “learning by confusion” to study phase transitions including topological order of the Kitaev chain. Unsupervised approaches include the use of diffusion maps [33] and topology preserving data generation [34]. Of particular relevance to our work are the papers [35, 13] that used convolutional neural networks and supervised learning to predict  $U(1)$  topological invariants. This work was later extended to an unsupervised setting in [14, 36] by incorporating the scheme of learning by confusion and augmenting data using topology preserving deformations.

### 3 Learning Multiband Chern Numbers

The band structure of the topological insulators we want to consider here is described by so-called Bloch Hamiltonians  $H(k)$  which are maps from the Brillouin zone to the space of  $M \times M$  complex Hermitian matrices. The Brillouin zone is the space of momenta  $k$  of the electrons which is periodic in each dimension. At each point  $k$  in the Brillouin zone, we consider the eigenvectors  $v_n(k) \in \mathbb{C}^M$ ,  $n = 1, \dots, N$ , of the Bloch Hamiltonian with negative eigenvalues since these correspond to the bands occupied by electrons in the material.

#### 3.1 Chern numbers for topological insulators

A nontrivial Chern number means that it is impossible to find smoothly varying eigenvectors over the entire Brillouin zone. In two dimensions, it is defined

via

$$C = \frac{1}{2\pi i} \int_{BZ} \text{Tr} [\mathcal{F}(k)] d^2 k, \quad (1)$$

where  $\mathcal{F}$  is an  $N \times N$ -matrix known as the non-abelian Berry curvature defined by

$$\mathcal{F} = \partial_{k_x} \mathcal{A}_y(k) - \partial_{k_y} \mathcal{A}_x(k) + [\mathcal{A}_x(k), \mathcal{A}_y(k)]. \quad (2)$$

Here,  $\mathcal{A}_\mu(k)$ ,  $\mu = x, y$  is the non-abelian Berry connection, another  $N \times N$ -matrix whose components are  $\mathbb{C}^2$ -vectors given by

$$[\mathcal{A}_\mu(k)]_{n,m} = v_n(k)^\top \partial_{k_\mu} v_m(k) \quad (3)$$

in terms of the eigenvectors of the Bloch Hamiltonian with negative eigenvalues.

It can be shown that the Chern number defined by (1) is an integer and there are generalizations to higher dimensional Brillouin zones, on which we performed experiments, see Section 6.3.

In practice, we consider a discretization of the Brillouin zone into a rectangular grid with periodic boundary conditions, of which there are a total of  $N_x \times N_y = N_{\text{site}}$  grid points. On this grid, one can define the following discrete, integer Chern number  $\tilde{C}$  which converges to  $C$  for vanishing grid spacing [37]

$$\tilde{C} = \sum_{(i,j)} \text{Im Tr} \log W_{i,j}, \quad (4)$$

where  $W_{i,j} \in U(N)$  is the Wilson loop at grid point  $\vec{k} = (i, j)$ , defined by

$$W_k = W_{i,j} = U_{i,j}^x U_{i-1,j}^y U_{i-1,j-1}^x U_{i,j-1}^y \quad (5)$$

in terms of the link matrices  $U_{i,j}^x, U_{i,j}^y \in \mathbb{C}^{N \times N}$ . These links capture the overlap between the eigenvectors of the Bloch Hamiltonians of neighboring grid points and have components

$$[U_{i,j}^x]_{m,n} = v_m(k_{i,j})^\top v_n(k_{i-1,j}) \quad (6)$$

$$[U_{i,j}^y]_{m,n} = v_m(k_{i,j})^\top v_n(k_{i,j-1}). \quad (7)$$

The links are discrete analogues of the operator  $\exp(i\mathcal{A}(k)dk)$ . The Wilson loops correspond to closed  $1 \times 1$  loops of the link variables. In higher dimensions, there are several Wilson loops  $W_k^\gamma$  per grid point  $k$  which are aligned with different directions  $\gamma$  in the lattice.

The learning task we will study in this article is to predict the discrete Chern number  $\tilde{C} \in \mathbb{Z}$  given the

Wilson loops  $W_{i,j} \in \mathbb{C}^{N \times N}$  on the lattice. One of our models also uses the links as additional input. Although the Chern number is given by the innocuous-looking equation (4), learning it is not straightforward as detailed in Section 3.3. We will show that the main reason for the difficulty of learning (4) lies in the gauge invariance of  $\tilde{C}$ .

### 3.2 Gauge symmetry

All topological indices, including the Chern number, are invariant under the gauge group  $U(N)$ . Gauge transformations are local symmetries, i.e. at each lattice point  $i, j$  they act with a different group element  $\Omega_{i,j} \in U(N)$  by

$$U_{i,j}^{x,y} \rightarrow (\Omega_{i,j})^\dagger U_{i,j}^{x,y} \Omega_{i+1,j} \quad (8)$$

$$W_{i,j}^\gamma \rightarrow \Omega_{i,j}^\dagger W_{i,j}^\gamma \Omega_{i,j}, \quad (9)$$

where  $\dagger$  denotes Hermitian conjugation. Hence, the total symmetry group is  $U(N)^{N_{\text{site}}}$ .

The gauge symmetry of the system implies the equivalence relation

$$W \sim \Omega^\dagger W \Omega \quad \forall \Omega \in U(N) \quad (10)$$

on the set of Wilson loops at each grid point. According to the spectral theorem, there is exactly one diagonal matrix in each equivalence class (group orbit) with elements in  $U(1)$ , up to reordering of the diagonal elements. Therefore, the set of equivalence classes for this relation is given by  $U(1)^N / S_N$ , the set of diagonal unitary  $N \times N$ -matrices up to permutation of the diagonal elements. This fact has been used in the construction of gauge equivariant spectral flows [22]. We will exploit it below to prove our universal approximation theorem and simplify the data augmentation process.

### 3.3 Learning Chern numbers using ResNets

Using the fact that  $\text{Tr} \log(X) = \log \det(X)$ , it follows that the Chern number defined in (4) can be written as a sum over  $\text{Im} \log \det(W)$ . As a warmup to predicting Chern numbers, we start by considering the simpler problem of predicting determinants of  $N \times N$  real matrices  $A$ .

We construct a dataset containing  $N \times N$  matrices with elements sampled from a uniform distribution

Table 1: Relative error  $\delta$  for linear MLP and bilinear residual architectures predicting the determinant of real  $4 \times 4$  matrices with uniform random elements in  $[0, 1]$ . Standard MLP architecture fails to learn the determinant relation.

Architecture	Layers	$\delta$
MLP	2	1.02
	3	1.02
Bilinear	2	0.01
	3	0.01

on the unit interval  $[0, 1]$ . As a baseline, we use a naive multi layer perceptron (MLP) with residual connections  $f : \mathbb{R}^{N^2} \rightarrow \mathbb{R}$ , taking the matrix elements as input, and predicting the determinant value.

The determinant of an  $N \times N$  matrix can be expressed as an order  $N$  polynomial in the matrix elements. For example, the determinant of a  $4 \times 4$  matrix  $A_{ij}$  is given by the fourth order expression

$$\det(A) = \sum_{i,j,k,l=1}^4 \epsilon^{ijkl} A_{1i} A_{2j} A_{3k} A_{4l}, \quad (11)$$

where  $\epsilon$  is the totally antisymmetric Levi-Cevita tensor.

Inspired by the functional form of the determinant in equation (11), we consider higher order layers with structure

$$A_{ij}^{\text{out}} = \sum_{k_1, \dots, k_{2R}} \theta_{ij}^{k_1 \dots k_{2R}} A_{k_1 k_2}^{\text{in}} \dots A_{k_{2R-1} k_{2R}}^{\text{in}}, \quad (12)$$

where  $R$  is the number of factors of  $A$  in the layer, and  $\theta_{ij}^{k_1 \dots k_{2R}}$  are learnable parameters. An architecture containing layers with  $R = 2$  will be referred to as bilinear. As the number of parameters grows quickly with order  $R$ , we use layers of order  $R \leq 4$  and construct higher order terms by composition of multiple layers. For example, two layers of order  $R = 3$  and  $R = 2$  will contain terms of order 2, 3 and 6 when using residual connections.

Predicted determinants  $f(A)$  are evaluated against the target determinant value  $\det(A)$  using absolute relative error  $\delta = |f(A) - \det(A)| / |\det(A)|$ . Table 1 shows the failure of a residual MLP architecture to learn the determinant of  $4 \times 4$  real matrices with uniformly distributed elements on  $[0, 1]$ , whereas a bilinear architecture with layers of order 2 can achieve low relative error.

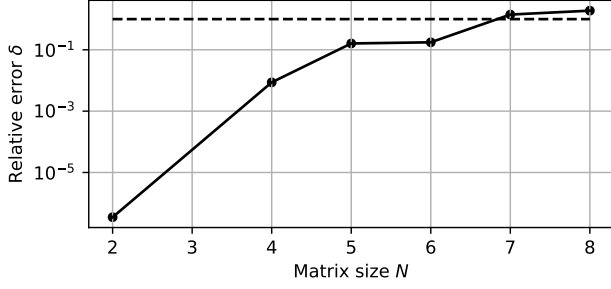


Figure 1: Best relative error of predicted matrix determinants for polynomial architectures as a function of increasing matrix size. The ablations include layers up to order 4. Dashed line indicates relative error of a mean predictor. Architectures considered include layers of order  $\leq 4$ , and depth  $\leq 4$ , containing terms of up to order 16 by composition.

Even though these higher order layers provide an architecture that is expressive enough for determinants in small dimensions, they quickly run into issues for larger matrices. Figure 1 shows that for matrix sizes corresponding to band size  $\geq 4$ , learning the determinant becomes prohibitively hard without better model priors.

## 4 Network Architecture

As demonstrated in the previous section, even hand-crafted polynomial architectures fail to learn a simplified version of the Chern number. Motivated by the performance of our gauge equivariant networks, we propose that this is due to the size of the gauge symmetry present in this problem. Since the Wilson loops at each site can be transformed independently, the total symmetry group is  $U(N)^{N_{\text{site}}}$ , a exponentially larger group than even for more traditional group equivariant networks.

The input data in our network is the set of discretized Wilson loops  $W_k^\gamma \in U(N)$  and all equivariant layers in our setup operator on tensors of this form. The index  $\gamma$  counts the number of different orientations of the Wilson loops per site (in 2D, there is only one) for the input and serves as a general channel index in deeper layers. Hence, our layers operate on complex tensors of the shape  $N_{\text{ch}} \times N_{\text{sites}} \times N \times N$ .

### 4.1 Gauge equivariant layers

Our model is composed of the following equivariant layers which were introduced in [15] as well as our new gauge equivariant normalization layer.

#### GEBl (Gauge Equivariant Bilinear Layers)

Given an input tensor  $W_k^\gamma$ , the layer computes a local quantity per site as

$$W_k'^\gamma = \sum_{\mu, \nu} \alpha_{\gamma\mu\nu} W_k^\mu W_k^\nu, \quad (13)$$

where  $W'$  has  $N_{\text{out}}$  channels and  $\alpha_{\gamma\mu\nu} \in \mathbb{C}^{N_{\text{in}} \times N_{\text{in}} \times N_{\text{out}}}$  are trainable parameters. Using (9), it can easily be checked that this layer is equivariant. In practice, GEBl includes also a linear and a bias term which are obtained by enlarging  $W$  with its Hermitian conjugate and the identity matrix. In order to merge two branches of the network, two different  $W$  can also be used on the right-hand side.

#### GEAct (Gauge Equivariant Activation Layers)

Given a tensor  $W_k^\gamma$ , the layer maintains channel size  $N_{\text{in}}$  and serves as an equivariant nonlinearity defined by

$$W_k'^\gamma = \sigma(\text{Tr} W_k^\gamma) W_k^\gamma, \quad (14)$$

where  $\sigma$  is a usual activation function. In Section 5, we prove a universal approximation theorem for a certain type of  $\sigma$ . In practice, we use  $\sigma(z) = \text{ReLU}(\text{Re}z)$  to avoid gradient vanishing, hence referring to this layer also as GEReLU.

#### GEConv (Gauge Equivariant Convolution Layers)

This is the only layer in our setup which introduces interactions between neighboring points. It is also the only layer for which the link variables  $U_k^\gamma$  are used. Given a tuple  $(U_k^\mu, W_k^\gamma)$ , the layer performs a convolution as

$$W_k'^\gamma = \sum_{\mu, d} \sum_{\sigma} \omega_{\mu d \gamma \sigma} (U_{k+d\hat{\mu}}^{d\mu})^\dagger W_{k+d\hat{\mu}}^\sigma U_k^{d\mu}, \quad (15)$$

where  $U_k^{d\mu} = U_k^\mu \dots U_{k+(d-1)\hat{\mu}}^\mu$  and  $d\hat{\mu}$  is the length- $d$  vector in the  $\mu$  direction in the lattice. The output  $W'$  of this layer has the shape  $N_{\text{out}} \times N_{\text{site}} \times N \times N$  and  $\omega$  are trainable weights of shape  $\text{dim} \times d \times N_{\text{out}} \times N_{\text{in}}$ . Note that this layer does not update the links. Using the transformations (8) and (9), one can check that this layer is equivariant as well. When we take a zero convolution kernel size, the layer degenerates into an equivariant linear layer that is completely local.

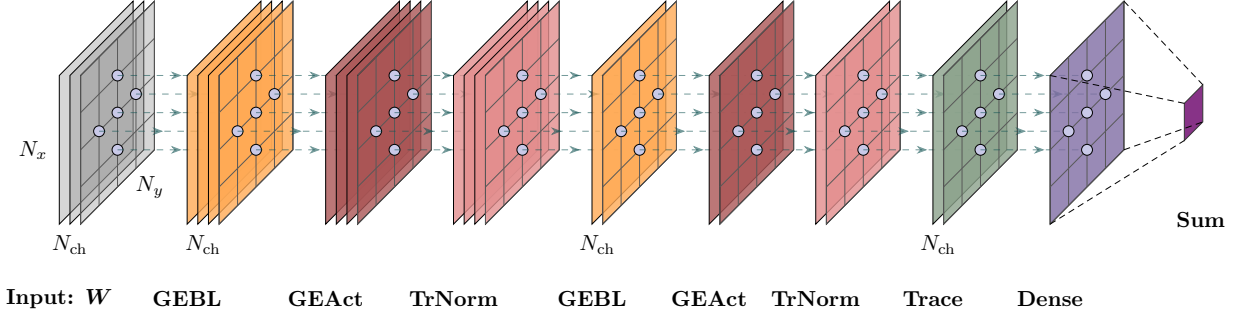


Figure 2: Architecture of GEBLNet. In this figure, the rectangles represent the spatial grid, and the number of layers ( $N_{\text{ch}}$ ) represents the number of channels ( $\gamma$ ). Each circle represents a site on the grid, and quantities on different sites do not interact with each other, until the last summation on grids.

**Trace Layer** Given a tensor  $W_k^\gamma$ , this layer maintains the channel size and takes the trace of the fluxes as

$$T_k^\gamma = \text{Tr}W_k^\gamma. \quad (16)$$

Since the trace is invariant under the transformations (9), this layer renders the features gauge invariant. The output has the shape  $N_{\text{in}} \times N_{\text{site}}$ .

**Dense Layer** After the trace layer, we perform a real valued linear layer on  $T_k$  as

$$T'_k = w_{\text{Re}} \cdot \text{Re}(T_k) + w_{\text{Im}} \cdot \text{Im}(T_k) + b, \quad (17)$$

where  $w_{\text{Re}}$ ,  $w_{\text{Im}}$  and  $b$  are trainable parameters. The output features have shape  $N_{\text{out}} \times N_{\text{site}}$ . Note that we only transform gauge invariant features with this layer since it does not respect the gauge symmetry.

**TrNorm (Trace Normalization Layers)** The bilinear GEBL-layers introduced above quickly lead to training instabilities when stacked deeply, as demonstrated in Section 6 below. To solve this problem, we introduce a novel gauge-equivariant normalization layer which we insert after the nonlinearities. Given an input tensor  $W_k^\gamma$ , this layer maintains the channel size and performs a channel-wise normalization as

$$W_k'^\gamma = \frac{1}{|\text{mean}_\gamma\{\text{Tr}W_k^\gamma\}|} W_k^\gamma. \quad (18)$$

This operation is gauge equivariant since the prefactor is gauge invariant. After the normalization, the output features  $W'$  satisfy  $\text{mean}_\gamma\{\text{Tr}W_k'^\gamma\} = e^{i\phi_k}$  for some  $\phi_k \in \mathbb{R}$ .

## 4.2 Network Architecture

We now use the layers introduced in the previous section to construct three different equivariant network architectures.

**GEBLNet (Gauge Equivariant Bilinear Network)** GEBLNet is a model that only operates locally, i.e. the inputs are the fluxes  $W_k^\gamma$  alone, and features at different sites only interact with each other in the final sum. It processes the fluxes through repeated blocks of GEBL, GEAct, and TrNorm layers. The outputs are then aggregated through a Trace layer, followed by a dense and a summation over sites to produce the prediction on the Chern number. This is our primary model to study. An example structure is shown in Figure 2.

**GEConvNet (Gauge Equivariant Convolutional Network)** GEConvNet is a model that features GEConv layers, therefore takes both the links ( $U^\mu$ ) and the fluxes ( $W^\gamma$ ) as input. Each GEBL-GEAct-TrNorm block, similar to that of GEBLNet, is paralleled by a GEConv-GEAct-TrNorm block, with their outputs combined through a subsequent GEBL layer. This process is repeated through several iterations, after which the resulting output is passed to the Trace-Dense- and sum sequence to produce the final prediction. An example structure is shown in Figure 9 in Appendix D.

**TrMLP (Trace Multilayer Perceptron)** As a baseline for two-dimensional grids, we also intro-

duce a Trace Multilayer Perceptron. This model takes only  $W^\gamma$  as inputs, extracts a characteristic vector  $(\text{Tr}(W_k^\gamma)^1, \dots, \text{Tr}(W_k^\gamma)^N)$  for some  $N$  per site and then applies an MLP on this vector, followed by a summation over sites for prediction. Its motivation and feasibility will be discussed in Section 5.

## 5 Theoretical Foundations of the Model

In this section we will present a universal approximation theorem for our models. We focus on GEBLNet, whose inputs are solely  $W_k$ . Recalling the equivalence relation (10), the local quantity is in fact a class function on the gauge group  $U(n)$ , which is defined as follows:

**Definition 1.** A (complex) class function on a Lie group is a function  $f : G \rightarrow \mathbb{C}$  such that:

$$f(ghg^{-1}) = f(h), \quad \forall g, h \in G \quad (19)$$

For compact Lie groups any continuous function on  $G$  is automatically square integrable due to the finiteness of the Haar measure. Hence, the space of class functions is a subset of  $L^2(G)$ . We will henceforth denote this subspace by  $L^2_{class}(G)$ .

We now present our main theoretical result, which shows our model's capability to learn an arbitrary class function.

**Theorem 1 (Universal Approximation Theorem).**

*For a compact Lie group  $G$ , and with the nonlinearity  $\sigma$  in GEAct taking the form  $\tilde{\sigma} \circ \text{Re}$ , where  $\sigma$  is bounded and non-decreasing, GEBLNet could approximate any class function on  $G$ .*

The full proof is given in Appendix C. Here we present a brief sketch of it. To this end we begin by introducing some properties of class functions.

**Theorem 2.** *The space of symmetric polynomials  $\{s_k\}$  over eigenvalues  $\{\lambda_k\}$  forms an orthonormal basis of  $L^2_{class}(G)$ .*

*Proof.* Follows directly from the Peter-Weyl theorem and the expansion of class functions in terms of irreducible characters.  $\square$

Furthermore, consider the set of polynomials over eigenvalues of  $g$ :  $\{p_k(\lambda_1, \dots, \lambda_n) = \sum_i \lambda_i^k\}$ . In our setting these polynomials can be identified with the set of traces of group elements of the form  $\text{Tr}g^k$ . Using Newton's identities for symmetric polynomials,

$$ke^k = \sum_{j=1}^k (-1)^{j-1} e_{k-j} p_j, \quad e_k = \sum_{\sum_n k_n=k} \prod \lambda_i^{k_i}, \quad (20)$$

one may deduce the following

**Corollary 3.** *The space  $\bigcup_M \{f(\text{Tr}g, \dots, \text{Tr}g^M)\} \cap L^2(G)$  is dense in  $L^2_{class}(G)$ .*

We are now ready to sketch the proof of Theorem 1.

*Sketch of Proof.* Consider a network with  $M$  GEBL layers and sufficient width. One can show that the output of such a network can approximate any function of the form

$$w_i \sigma(\text{Re} \sum_{j=0}^{2^M} \alpha_{ij} \text{Tr}g^j) (\sum_{j=0}^{2^M} \alpha_{ij} \text{Tr}g^j) + b. \quad (21)$$

However, this is equivalent to a one-layer MLP on the polynomials  $(\text{Tr}g, \dots, \text{Tr}g^{2^M})$ . Therefore it can approximate any function in  $\{f(\text{Tr}g, \dots, \text{Tr}g^{2^M})\} \cap L^2(G)$ . By Corollary 3, we conclude that eq.(21) can approximate any function in  $L^2_{class}(G)$ .  $\square$

We refer to Appendix C for the complete proof.

## 6 Experiments

To assess the performance of our gauge-equivariant neural network, we conducted experiments on synthetic datasets with varying grid sizes and distributions. Unless specified, the dataset is based on 2D grids. In this case, sample data shall have the form  $(U_k^x, U_k^y, W_k)_k$ .

### 6.1 Data Generation

**General Dataset** The data generation pipeline consists of two main steps. Given a grid size  $N_x \times N_y$ , we first generate random link variables using the following algorithm:

1. For  $\mu = x, y$ , draw  $A_k^\mu \sim \mathcal{N}(0, 1)^{N \times N}$ .

2. Perform a QR decomposition on  $A_k^\mu$ , decomposing it into the product of a unitary matrix  $U_k^\mu$  and a semi-definite matrix  $\Sigma_k^\mu$ ,  $A_k^\mu = U_k^\mu \Sigma_k^\mu$ .
3. Use  $U_k^\mu$  as the link variable for site  $k$  in direction  $\mu$ .

It can be shown that the distribution of the links generated in this way is uniform on  $U(N)$ , i.e. the random variables  $U$  and  $gU$  are identically distributed for all  $g \in U(N)$ . See Appendix B for details.

In the next step, we compute the fluxes  $W_k$  using (5) and the discrete Chern number  $\tilde{C}$  using (4). Ultimately, this yields a dataset of data-value pairs  $((U_k^\mu, W_k^\gamma), \tilde{C})$ . We generate the training samples continuously during training to avoid overfitting.

**Diagonal Dataset** For some of our experiments, we require control over the distribution of the Chern numbers in our training data. To this end, we employ a different data generation strategy. Due to the invariance of our model under gauge transformations, training samples which lie in the same gauge orbit are equivalent in the sense that the parameter updates they induce are the same. This implies that we can select an arbitrary element along the gauge orbit for training. As discussed in Section 3.2, there is always a diagonal matrix with  $U(1)$ -valued components in the orbit. Therefore, by training on these matrices in  $U(1)^N$  and manipulating the distribution of the diagonal values, we can generate datasets with different distributions of Chern numbers. Note that networks trained on these datasets of course generalize to non-diagonal Wilson loops since they are gauge invariant. Detailed discussions are provided in Appendix B.

## 6.2 Training and Evaluation

We adopt two loss functions for our training: the global loss  $L_g$  and the standard deviation loss  $L_{std}$ . Specifically, given the network  $f(W)$  and the Chern number  $\tilde{C}$ ,  $L_g$  calculates  $\|f(W) - \tilde{C}\|_1$ . Meanwhile,  $L_{std}$  evaluates the entrywise standard deviation of the network output after the dense layer, denoted as  $(g(W_k))_k$ , namely  $\|\max(\{\text{std}(g(W_k)_k), \delta\}) - \delta\|_1$ , where  $\delta$  is a hyperparameter, set to 0.5 by default. The standard deviation loss is necessary to prevent the model from collapsing to only zero outputs, since

Table 2: Accuracy of GEBLNet trained and evaluated on a  $5^2$  grid.

Bands	4	5	6	7	8
Accuracy (%)	95.9	94.0	93.8	91.7	52.5

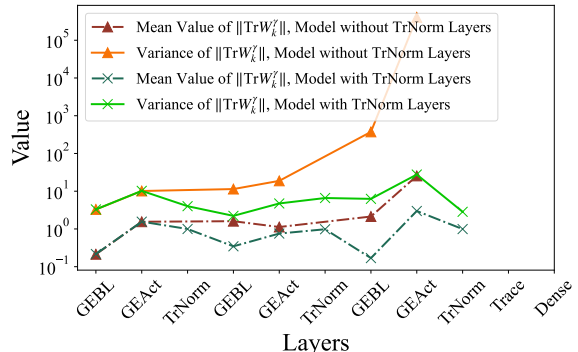


Figure 3: Comparison of statistics of  $\|\text{Tr}W_k^{\gamma}\|$  across each layer, between two training runs on a  $5 \times 5$  grid, with 4 filled bands. The two runs have identical configurations, except for the implementation of TrNorm Layers.

it forces the model to output locally differed quantities. This is particularly relevant for the training on trivial topologies only, as described below. The total loss function  $L_{total}$  adds these two terms,  $L_{total} = L_g + L_{std}$ .

For evaluation, we compute the accuracy by rounding the network output  $f(W)$  to the nearest integer and comparing it with the Chern number  $\tilde{C}$ , unless otherwise specified.

**Baseline Model Configuration** For the main architecture GEBLNet, we set a baseline model configuration, whose GEBl layers and hyperparameters are listed in Table 4 in the appendix.

## 6.3 Experimental Results

**Model Comparison** For a basic model comparison, we train GEBLNet, GEConvNet, and TrMLP on 2D grids to learn Chern numbers by training on non-diagonal data. We find that GEBLNet outperforms the other models in both accuracy and robustness, see Figure 10 in Appendix D.

Using a benchmark grid size of  $5 \times 5$  and  $N = 4$  filled bands, GEBLNet achieved approximately 95% accu-

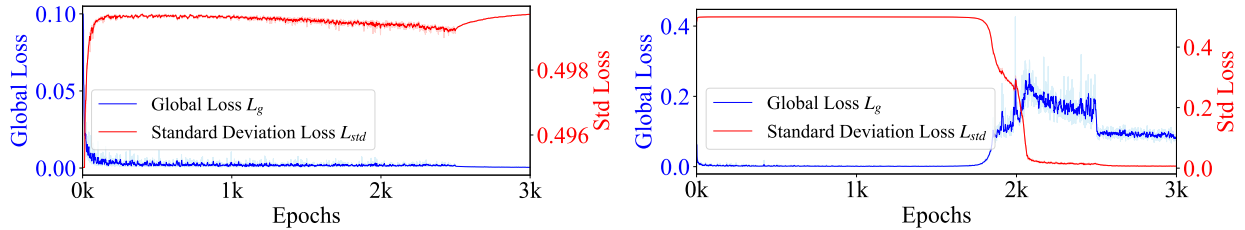


Figure 4: Comparison of global and standard deviation loss on validation data between the same two runs learning on only zero Chern numbers, as shown in Figure 3. The former, without TrNorm layers, collapses to zero local quantities everywhere, hence having a lower  $L_g$  on trivial samples than the latter with TrNorm layers. Nevertheless, the former could not generalize to nontrivial cases. In contrast, the latter, with TrNorm layers, succeeds in learning global quantities and local differences simultaneously.

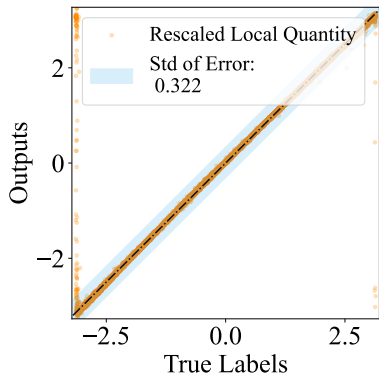


Figure 5: Comparison of rescaled local outputs with local true values. Points closer to the reference line  $y = x$  indicate higher accuracy in capturing local quantities.

racy across different seeds, demonstrating strong robustness. In contrast, GEConvNet struggled to learn correct results with positive kernel sizes, likely due to redundant information. We also tested a degenerate GEConvNet with kernel size 0 (a local network) which performed better than its non-local counterpart, but it remained less robust than GEBLNet. TrMLP was highly sensitive to initialization, frequently encountering gradient explosions, and most successful runs exhibited low accuracy.

A complexity-accuracy comparison in Figure 10 in the appendix demonstrates the balance achieved by the baseline model, which performed consistently well while maintaining efficiency. Additionally, tests on increasing band sizes (Table 2) show that the baseline model effectively learns Chern numbers up to 7 bands, retaining high accuracy and robustness.

**Training on Trivial Topologies** In order to test the generalization properties of our model, we train exclusively on topologically trivial samples. To achieve this, non-trivial samples were manually filtered out

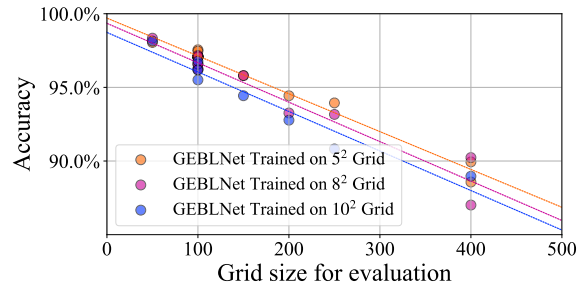


Figure 6: Comparison of model accuracy across different grid sizes. Each run, represented by markers of the same color, has identical configurations, but is trained on grids of a different size. Each line represents a linear regression on the corresponding run.

during data generation, turning  $L_g$  effectively into  $\|f(W)\|_1$ .

A naive GEBLNet model without TrNorm layers can learn the Chern number for up to 3 bands but fails for 4 bands and above, mostly outputting zero local quantities except for a few random seeds. Analyzing the statistics of output traces per layer (Figure 3) reveals that variance accumulates across layers, reaching  $10^5$  after the final GEAct layer, causing numerical instability and vanishing gradients.

Introducing TrNorm layers mitigates this issue, stabilizing the variance and enabling the model to learn Chern number of systems with more than 4 bands. Figure 4 compares the loss curves between models with and without TrNorm layers, demonstrating the effectiveness of this modification.

Furthermore, training solely on trivial samples limits the model to learning the Chern number up to a global, sample independent, rescaling factor, i.e.  $f(W) \approx k\tilde{C}$  for some  $k$ . To evaluate on general samples, we compute the rescaling factor  $R_{\text{scale}} = \text{mean}(\tilde{C})/\text{mean}(f(W))$  using a large set of non-trivial samples and scale the output as  $R_{\text{scale}}f(W)$ .

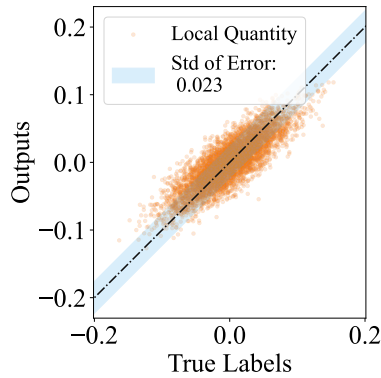


Figure 7: Comparison of rescaled local outputs with local true values.

The training results demonstrated prediction accuracy comparable to that of training on general datasets, as detailed in Table 3 in Appendix B, we obtain an accuracy of approximately 94.1% on four bands, comparable to 95.9% for training on data which includes non-trivial Chern numbers. Meanwhile, Figure 5 shows the model’s ability to capture local quantities accurately.

**Larger grids** Due to its local structure, GEBLNet can process samples of arbitrary grid sizes. We evaluate its generalization abilities by testing samples on larger grids using a baseline model trained on smaller grids. The results, shown in Figure 6, indicate that our models show excellent generalization ability to larger grid sizes. The moderate accuracy decrease we observe is approximately linearly with the number of grid sites, likely due to accumulating errors. Training on larger grids slightly improves performance but comes at a considerable computational cost.

**Learning higher-dimensional Chern numbers** We extended the task to learning Chern numbers to 4D grids, whose definitions are significantly more complex than the 2D case (see Appendix A). Furthermore, instead of a single flux  $W_k$ , there are  $C_4^2 = 6$  Wilson loops per site in 4D. Since for higher dimensions, the discrete approximation to the Chern number is not necessarily an integer, we cannot use the accuracy for evaluation. Therefore, we use the MAE (global loss  $L_g$ ) instead, see Figure 11 in Appendix D. With an MAE of around 0.25, our models can predict these higher-dimensional Chern numbers well within rounding errors. Figure 7 demonstrates the predictions of local quantities, showing good agreement with the targets.

## Acknowledgments

We want to thank David Müller and Daniel Schuh for inspiring discussions. The work of J.G. and D.P. is supported by the Wallenberg AI, Autonomous Systems and Software Program (WASP) funded by the Knut and Alice Wallenberg (KAW) Foundation. M.G. acknowledges support from KAW through the Wallenberg Centre for Quantum Technology (WACQT). The computations were enabled by resources provided by the National Academic Infrastructure for Supercomputing in Sweden (NAISS), partially funded by the Swedish Research Council through grant agreement no. 2022-06725.

## References

- [1] Jan E. Gerken et al. “Geometric Deep Learning and Equivariant Neural Networks”. In: *Artificial Intelligence Review* (June 2023). ISSN: 1573-7462. DOI: [10.1007/s10462-023-10502-7](https://doi.org/10.1007/s10462-023-10502-7). arXiv: [2105.13926](https://arxiv.org/abs/2105.13926).
- [2] Erik J. Bekkers et al. “Roto-Translation Covariant Convolutional Networks for Medical Image Analysis”. In: *Medical Image Computing and Computer Assisted Intervention – MICCAI 2018*. Ed. by Alejandro F. Frangi et al. Lecture Notes in Computer Science. Cham: Springer International Publishing, 2018, pp. 440–448. ISBN: 978-3-030-00928-1. DOI: [10.1007/978-3-030-00928-1\\_50](https://doi.org/10.1007/978-3-030-00928-1_50).
- [3] Alexander Bogatskiy et al. “Lorentz Group Equivariant Neural Network for Particle Physics”. In: *Proceedings of the 37th International Conference on Machine Learning*. Ed. by Hal Daumé III and Aarti Singh. Vol. 119. Proceedings of Machine Learning Research. PMLR, 2020, pp. 992–1002. arXiv: [2006.04780](https://arxiv.org/abs/2006.04780).
- [4] Alexandre Duval et al. *A Hitchhiker’s Guide to Geometric GNNs for 3D Atomic Systems*. Dec. 2023. DOI: [10.48550/arXiv.2312.07511](https://arxiv.org/abs/10.48550/arXiv.2312.07511). arXiv: [2312.07511](https://arxiv.org/abs/2312.07511) [cs, q-bio].
- [5] Joel E Moore. “The birth of topological insulators”. In: *Nature* 464.7286 (2010), pp. 194–198. DOI: [10.1038/nature08916](https://doi.org/10.1038/nature08916).
- [6] M. Z. Hasan and C. L. Kane. “Colloquium: Topological insulators”. In: *Rev. Mod. Phys.* 82 (4 2010), pp. 3045–3067. DOI: [10.1103/RevModPhys.82.3045](https://doi.org/10.1103/RevModPhys.82.3045). URL: <https://link.aps.org/doi/10.1103/RevModPhys.82.3045>.
- [7] Qing Lin He et al. “Topological spintronics and magnetoelectronics”. In: *Nature materials* 21.1 (2022), pp. 15–23. DOI: [10.1038/s41563-021-01138-5](https://doi.org/10.1038/s41563-021-01138-5).
- [8] Ling Lu, John D. Joannopoulos, and Marin Soljačić. “Topological photonics”. In: *Nature Photonics* 8.11 (2014), pp. 821–829. ISSN: 1749-4893. DOI: [10.1038/nphoton.2014.248](https://doi.org/10.1038/nphoton.2014.248). URL: <https://doi.org/10.1038/nphoton.2014.248>.

- [9] Kyung-Hwan Jin et al. “Topological quantum devices: a review”. In: *Nanoscale* 15.31 (July 2023). doi: [10.1039/d3nr01288c](https://doi.org/10.1039/d3nr01288c).
- [10] Paolo Zanardi and Mario Rasetti. “Holonomic quantum computation”. In: *Physics Letters A* 264.2-3 (1999), pp. 94–99.
- [11] Chetan Nayak et al. “Non-Abelian anyons and topological quantum computation”. In: *Rev. Mod. Phys.* 80 (3 2008), pp. 1083–1159. doi: [10.1103/RevModPhys.80.1083](https://doi.org/10.1103/RevModPhys.80.1083). URL: <https://link.aps.org/doi/10.1103/RevModPhys.80.1083>.
- [12] Carlo W. J. Beenakker. “Search for Majorana fermions in superconductors”. In: *Annual Review of Condensed Matter Physics* 4 (2013), pp. 113–136. doi: [10.1146/annurev-conmatphys-030212-184337](https://doi.org/10.1146/annurev-conmatphys-030212-184337). URL: <https://doi.org/10.1146/annurev-conmatphys-030212-184337>.
- [13] Ning Sun et al. “Deep learning topological invariants of band insulators”. In: *Phys. Rev. B* 98 (8 2018), p. 085402. doi: [10.1103/PhysRevB.98.085402](https://doi.org/10.1103/PhysRevB.98.085402). URL: <https://link.aps.org/doi/10.1103/PhysRevB.98.085402>.
- [14] Oleksandr Balabanov and Mats Granath. “Unsupervised learning using topological data augmentation”. In: *Phys. Rev. Res.* 2 (1 2020), p. 013354. doi: [10.1103/PhysRevResearch.2.013354](https://doi.org/10.1103/PhysRevResearch.2.013354). URL: <https://link.aps.org/doi/10.1103/PhysRevResearch.2.013354>.
- [15] Matteo Favoni et al. “Lattice Gauge Equivariant Convolutional Neural Networks”. In: *Physical Review Letters* 128.3 (Jan. 2022), p. 032003. doi: [10.1103/PhysRevLett.128.032003](https://doi.org/10.1103/PhysRevLett.128.032003). arXiv: [2012.12901](https://arxiv.org/abs/2012.12901).
- [16] Michael M. Bronstein et al. *Geometric Deep Learning: Grids, Groups, Graphs, Geodesics, and Gauges*. Apr. 2021. arXiv: [2104.13478](https://arxiv.org/abs/2104.13478) [cs, stat].
- [17] Maurice Weiler et al. *Equivariant and Coordinate Independent Convolutional Networks. A Gauge Field Theory of Neural Networks*. 2023. doi: [10.1142/14143](https://doi.org/10.1142/14143).
- [18] Miranda C. N. Cheng et al. “Covariance in Physics and Convolutional Neural Networks”. In: *arXiv:1906.02481 [hep-th, stat]* (June 2019). arXiv: [1906.02481](https://arxiv.org/abs/1906.02481) [hep-th, stat].
- [19] Taco S. Cohen et al. “Gauge Equivariant Convolutional Networks and the Icosahedral CNN”. In: *arXiv:1902.04615 [cs, stat]* (Feb. 2019). arXiv: [1902.04615](https://arxiv.org/abs/1902.04615) [cs, stat].
- [20] Pim de Haan et al. “Gauge Equivariant Mesh CNNs: Anisotropic Convolutions on Geometric Graphs”. In: *arXiv:2003.05425 [cs, stat]* (Mar. 2020). arXiv: [2003.05425](https://arxiv.org/abs/2003.05425) [cs, stat].
- [21] Gurtej Kanwar et al. “Equivariant Flow-Based Sampling for Lattice Gauge Theory”. In: *Physical Review Letters* 125.12 (Sept. 2020), p. 121601. doi: [10.1103/PhysRevLett.125.121601](https://doi.org/10.1103/PhysRevLett.125.121601).
- [22] Denis Boyda et al. “Sampling Using SU(N) Gauge Equivariant Flows”. In: *Physical Review D* 103.7 (Apr. 2021), p. 074504. doi: [10.1103/PhysRevD.103.074504](https://doi.org/10.1103/PhysRevD.103.074504).
- [23] Kim A. Nicoli et al. “Estimation of Thermodynamic Observables in Lattice Field Theories with Deep Generative Models”. In: *Physical Review Letters* 126.3 (Jan. 2021), p. 032001. doi: [10.1103/PhysRevLett.126.032001](https://doi.org/10.1103/PhysRevLett.126.032001).
- [24] Simone Bacchio et al. “Learning Trivializing Gradient Flows for Lattice Gauge Theories”. In: *Physical Review D* 107.5 (Mar. 2023), p. L051504. doi: [10.1103/PhysRevD.107.L051504](https://doi.org/10.1103/PhysRevD.107.L051504).
- [25] Ryan Abbott et al. “Sampling QCD Field Configurations with Gauge-Equivariant Flow Models”. In: *Proceedings of The 39th International Symposium on Lattice Field Theory — PoS(LATTICE2022)*. Vol. 430. SISSA Medialab, Apr. 2023, p. 036. doi: [10.22323/1.430.0036](https://doi.org/10.22323/1.430.0036). arXiv: [2208.03832](https://arxiv.org/abs/2208.03832).
- [26] Di Luo et al. “Gauge Equivariant Neural Networks for Quantum Lattice Gauge Theories”. In: *Physical Review Letters* 127.27 (Dec. 2021), p. 276402. doi: [10.1103/PhysRevLett.127.276402](https://doi.org/10.1103/PhysRevLett.127.276402). arXiv: [2012.05232](https://arxiv.org/abs/2012.05232).
- [27] Giuseppe Carleo et al. “Machine learning and the physical sciences”. In: *Reviews of Modern Physics* 91.4 (Dec. 2019). ISSN: 1539-0756. doi: [10.1103/revmodphys.91.045002](https://doi.org/10.1103/revmodphys.91.045002). URL: <http://dx.doi.org/10.1103/RevModPhys.91.045002>.
- [28] Juan Carrasquilla. “Machine learning for quantum matter”. In: *Advances in Physics: X* 5.1 (Jan. 2020), p. 1797528. ISSN: 2374-6149. doi: [10.1080/23746149.2020.1797528](https://doi.org/10.1080/23746149.2020.1797528). URL: <http://dx.doi.org/10.1080/23746149.2020.1797528>.
- [29] Mario Krenn et al. “Artificial intelligence and machine learning for quantum technologies”. In: *Phys. Rev. A* 107 (1 2023), p. 010101. doi: [10.1103/PhysRevA.107.010101](https://doi.org/10.1103/PhysRevA.107.010101). URL: <https://link.aps.org/doi/10.1103/PhysRevA.107.010101>.
- [30] Anna Dawid et al. *Modern applications of machine learning in quantum sciences*. 2023. arXiv: [2204.04198](https://arxiv.org/abs/2204.04198) [quant-ph]. URL: <https://arxiv.org/abs/2204.04198>.
- [31] Juan Carrasquilla and Roger G. Melko. “Machine learning phases of matter”. In: *Nature Physics* 13.5 (Feb. 2017), 431–434. ISSN: 1745-2481. doi: [10.1038/nphys4035](https://doi.org/10.1038/nphys4035). URL: <http://dx.doi.org/10.1038/nphys4035>.
- [32] Evert P. L. van Nieuwenburg, Ye-Hua Liu, and Sebastian D. Huber. “Learning phase transitions by confusion”. In: *Nature Physics* 13.5 (Feb. 2017), 435–439. ISSN: 1745-2481. doi: [10.1038/nphys4037](https://doi.org/10.1038/nphys4037). URL: <http://dx.doi.org/10.1038/nphys4037>.
- [33] Yanming Che et al. “Topological quantum phase transitions retrieved through unsupervised machine learning”. In: *Phys. Rev. B* 102 (13 2020), p. 134213. doi: [10.1103/PhysRevB.102.134213](https://doi.org/10.1103/PhysRevB.102.134213). URL: <https://link.aps.org/doi/10.1103/PhysRevB.102.134213>.
- [34] Mathias S. Scheurer and Robert-Jan Slager. “Unsupervised Machine Learning and Band Topology”. In: *Phys. Rev. Lett.* 124 (22 2020), p. 226401. doi: [10.1103/PhysRevLett.124.226401](https://doi.org/10.1103/PhysRevLett.124.226401). URL: <https://link.aps.org/doi/10.1103/PhysRevLett.124.226401>.

- [35] Pengfei Zhang, Huitao Shen, and Hui Zhai. “Machine Learning Topological Invariants with Neural Networks”. In: *Physical Review Letters* 120.6 (Feb. 2018). ISSN: 1079-7114. DOI: [10.1103/physrevlett.120.066401](https://doi.org/10.1103/physrevlett.120.066401). URL: <http://dx.doi.org/10.1103/PhysRevLett.120.066401>.
- [36] Oleksandr Balabanov and Mats Granath. “Unsupervised interpretable learning of topological indices invariant under permutations of atomic bands”. In: *Machine Learning: Science and Technology* 2.2 (2020), p. 025008. DOI: [10.1088/2632-2153/abcc43](https://doi.org/10.1088/2632-2153/abcc43).
- [37] Takahiro Fukui, Yasuhiro Hatsugai, and Hiroshi Suzuki. “Chern numbers in discretized Brillouin zone: efficient method of computing (spin) Hall conductances”. In: *Journal of the Physical Society of Japan* 74.6 (2005), pp. 1674–1677. DOI: [10.1143/JPSJ.74.1674](https://doi.org/10.1143/JPSJ.74.1674).

## A Higher Order Chern Numbers

In 3.1, we defined in (4) for two dimensional Brillouin zones the non-abelian Berry curvature as

$$\mathcal{F} = \partial_{k_x} \mathcal{A}_y(k) - \partial_{k_y} \mathcal{A}_x(k) + [\mathcal{A}_x(k), \mathcal{A}_y(k)].$$

For  $2n$  dimensional Brillouin zones, which are topologically equivalent to  $\mathbb{R}^{2n}/\mathbb{Z}^{2n}$ , there are  $P_{2n}^2$  different oriented planes, i.e. for every two directions  $k_\mu, k_\nu$ , there is a planar flux

$$W_k^{\mu,\nu} = U_k^\mu U_{k+\hat{\mu}}^\nu (U_{k+\hat{\nu}}^\mu)^\dagger (U_k^\nu)^\dagger. \quad (22)$$

It is easy to verify that  $W_k^{\mu,\nu} = (W_k^{\nu,\mu})^\dagger$ . Similarly, there is a planar curvature

$$\mathcal{F}_{\mu,\nu} = \partial_{k_\mu} \mathcal{A}_\nu(k) - \partial_{k_\nu} \mathcal{A}_\mu(k) + [\mathcal{A}_\mu(k), \mathcal{A}_\nu(k)]. \quad (23)$$

Where  $\mathcal{A}_\mu$  is similarly defined as in (3). We showed in 3.1 the definition of Chern numbers on a  $2D$  Brillouin zone in (1). For a  $2n$  dimensional Brillouin zone, a  $n_{th}$  order Chern number is defined as

$$C_n = \frac{1}{n! (2\pi i)^n} \int_{BZ} \text{Tr} [\mathcal{F}(k)^n] d^{2n} k. \quad (24)$$

Here,  $\mathcal{F}(k)^n$  represents a wedge product of differential forms  $\mathcal{F}_{\mu,\nu}(k) dk_\mu dk_\nu$ , which could be written equivalently as

$$\frac{1}{2^n} \sum_{\mu_1, \mu_2, \dots, \mu_{2n-1}, \mu_{2n}} \epsilon_{\mu_1, \mu_2, \dots, \mu_{2n-1}, \mu_{2n}} \prod_{t=1}^n \mathcal{F}_{\mu_{2t-1}, \mu_{2t}}(k). \quad (25)$$

It could be shown that  $C$  is always an integer,  $\forall n \geq 1$ .

In practice, since the fluxes  $W_k^{\mu,\nu}$  is an approximation of  $\exp(\mathcal{F}_{\mu,\nu})$ , we calculate the discrete version of higher order Chern numbers with the following equation

$$\tilde{C}_n = \frac{1}{n! (2\pi i)^n 2^n} \sum_k \sum_{\mu_1, \mu_2, \dots, \mu_{2n-1}, \mu_{2n}} \text{Tr} \epsilon_{\mu_1, \mu_2, \dots, \mu_{2n-1}, \mu_{2n}} \prod_{t=1}^n \log W_k^{\mu_{2t-1}, \mu_{2t}}. \quad (26)$$

When taking  $n = 1$ , Equation (26) coincides with (4). Since log function is analytical, which means could be represented by a power series, and  $(\Omega^\dagger W \Omega)^n = \Omega^\dagger W^n \Omega$ , we have

$$\tilde{C}(W_k^{\mu_{2t-1}, \mu_{2t}}) = \tilde{C}(\Omega^\dagger W_k^{\mu_{2t-1}, \mu_{2t}} \Omega), \quad \forall \Omega \in U(N)$$

This discretized Chern number is an integer only in the continuum limit, therefore we use the MAE (global loss  $L_g$ ) instead for evaluation.

## B Data Generation

### B.1 Uniform Distribution on $U(N)$ with QR Decomposition

In the experiments we generate  $U(N)$  with QR Decomposition on a matrix  $A \in \mathbb{C}^{N \times N}$ , whose entries have i.i.d.  $\mathcal{N}(0, 1)$  real and imaginary parts. We assume the algorithm to generate  $U$  from  $A$  is single-valued, i.e.  $U = f(A)$  for some function  $f : \mathbb{C}^{N \times N} \rightarrow U(N)$ . We show the "left invariance" of the random variable  $U$ .

**Proposition 4.**  $U$  and  $gU$  are identically distributed,  $\forall g \in G$ .

*Proof.* By definition,  $gU = f(gA)$ . Then it suffices to show  $gA$  and  $A$  are identically distributed.

For complex matrices, we consider the two bijections. The first one is  $p : A \rightarrow \begin{pmatrix} \text{Re}A \\ \text{Im}A \end{pmatrix}$ . Then  $p(gA) = \begin{pmatrix} \text{Re}gA & -\text{Im}gA \\ \text{Im}gA & \text{Re}gA \end{pmatrix} = \hat{g}p(A)$ . It is easy to verify  $\hat{g}$  is orthogonal. We then flatten the matrix with a vec operator

$$\text{vec}(A) = (A_{11}, A_{12}, \dots, A_{1N}, \dots, A_{M1}, \dots, A_{MN})$$

The following property is well known.

**Proposition 5 (Vec Operator Identity).**  $\text{vec}(gA) = (g \otimes I_N)\text{vec}(A)$

Where  $\otimes$  is the Kronecker product. Then  $\text{vec}(p(gA)) = (\hat{g} \otimes I_N)\text{vec}(p(A))$ . However,  $\text{vec}(p(A))$  is just  $(\text{Re}A_{ij}, \text{Im}A_{ij})$ , which follows the distribution  $\mathcal{N}(0, I_{2N^2})$ , and  $\hat{g} \otimes I_N$  is still orthogonal, it follows that

$$\text{vec}(p(gA)) \sim \mathcal{N}(0, (\hat{g} \otimes I_N)I_{2N^2}(\hat{g} \otimes I_N)^T) = \mathcal{N}(0, I_{2N^2})$$

Therefore  $\text{vec}(p(gA)) \sim \text{vec}(p(A))$ . By bijectivity,  $gA \sim A$ . □

### B.2 Diagonal Dataset

There is a equivalence relation among samples  $W_k$ :  $W_k \sim \Omega_k \tilde{W}_x \Omega_k^\dagger, \forall \Omega_k \in U(n), \forall k$ . Namely the equivalent classes of fluxes is a subset of  $(U(n)/\text{Ad})^{N_{\text{site}}}$ . By the isomorphism

$$U(n)/\text{Ad} \cong U(1)^n/S_n, \tag{27}$$

we could generate plaquettes  $W_k$  as diagonal matrices, i.e.  $W_k = \text{diag}\{e^{i\theta_k^1}, \dots, e^{i\theta_k^N}\}$ .

Notice that each link appears exactly twice in all plaquettes, once in itself, and once inverted. For example,  $U_k^x$  appears in itself in  $W_k$  and inverted in  $W_{k-\hat{y}}$ . Then we have:

$$\prod_k \det W_k = \prod_{\mu, k} \det U_k^\mu (\det U_k^\mu)^{-1} = 1$$

Specifically, since  $\sum_k \text{Im}(\log(\det W_k)) = \text{Im}(\log(\prod \det W_k)) \pmod{2\pi}$ , the discrete Chern number  $\tilde{C}$  is an integer.

**Proposition 6.**  $\tilde{C} = \frac{1}{2\pi} \sum_x F_x = n \in \mathbb{Z}$ .

Then the necessary condition for a set of plaquettes to be generated from some links is:

$$\prod_k \prod_\lambda e^{i\theta_k^\lambda} = e^{i \sum_k \sum_\lambda \theta_k^\lambda} = 1, \tag{28}$$



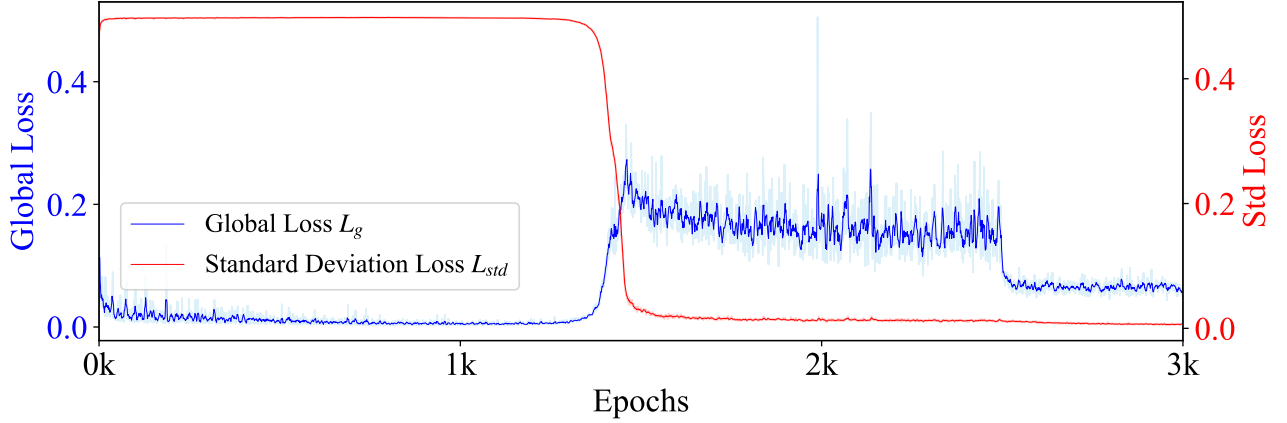


Figure 8: Global Loss and Standard Deviation Loss curve of the baseline model, trained on a diagonal, trivial dataset, to learn the Chern number on a  $5^2$  grid, with 4 filled bands.

Table 3: Accuracy of the same run in Figure 8, evaluated on non-diagonal, non-trivial data on a  $5 \times 5$  grid, with 4 filled bands.

Seeds	No.1	No.2	No.3	No.4
Accuracy	92.7%	94.3%	95.4%	93.8%

## C Proof of the Universal Approximation Theorem

Here we give the complete proof of Theorem 1, or, rather its stronger form in Theorem 7.

We consider the network architecture GEBLNet. Given the flux tensor  $W_k$ , we stack the identity and its Herimition conjugate to a second channel as

$$W_k^{\prime\gamma} = (W_{k,0}, W_{k,1}, W_{k,-1}) := (I, W_k, W_k^{-1}).$$

Afterwards we put it through several blocks, each containing three layers: GEBL, GEAct and TrNorm. In this section, we ignore TrNorm Layers, since they are introduced to boost training results. We call each block a “packed layer”.

After several packed layers we calculate the trace per-channel and add a linear layer (the “Dense layer”) in the end. The Dense layer acts on the real and imaginary parts separately. Then we take the sum over the site index (to calculate the topological invariant).

So the outputs have the following form:

$$W_k \mapsto w \cdot \hat{\sigma} \circ \text{GEBL}_n \circ \dots \circ \hat{\sigma} \circ \text{GEBL}_1(W_k) + b.$$

Where  $\hat{\sigma}(W_k^\gamma) = \sigma(\text{Tr}W_k^\gamma)W_k^\gamma$ . We denote the set of these functions by  $\mathcal{BLN}_\sigma(G)$ , where the subscript  $\sigma$  indicates the choice of activation function. We further denote by  $\mathcal{BLN}_\sigma^k(G)$  the subset of  $\mathcal{BLN}_\sigma(G)$  with  $k$  packed layers.

Since we attempted to learn local quantities  $F(W_k)$ , we omit the subscript  $k$ . Furthermore, we treat the flux  $W$  as an abstract element in the Lie group  $G$ , denoted as  $g$ . In this case where the input channel size is one, we propose the main result:

**Theorem 7 (Universal Approximation Theorem).** *For any activation function  $\sigma = \tilde{\sigma} \circ \text{Re}$ , where  $\tilde{\sigma}$  is bounded and non-decreasing,  $\mathcal{BLN}_\sigma(G)$  is dense in  $L_{class}^2(G)$ .*

The proof of this will require the following lemma.

**Lemma 8.**  $\mathcal{BLN}_\sigma^k(G)$  is dense in  $\{f(p_1, \dots, p_{2k}) : \|f\|_\infty < \infty\} \subset L^\infty(G)$ , where  $p_i = \text{Tr}g^i$ .

*Proof.* We prove this lemma by induction. For  $k = 1$ , the output has the following form

$$g \mapsto \left( \sum_{i=0}^2 \alpha_i^t g^t \right)_i \mapsto \omega_i \text{Tr} \sigma \left( \sum_{i=0}^2 \alpha_i^t g^t \right)_i + b.$$

Note that  $\text{Tr} \hat{\sigma}(\sum_{i=0}^2 \alpha_i^t g^t) = \sigma(\text{Re} \alpha_i^t p_t) \alpha_i^t p_t$ . For any channel index  $i$ , when taking only the real part (in other words, forcing  $w_{i, \text{Im}}$  in the dense layer to be zero), the output is simply

$$\sigma \left( \sum_t \text{Re} \alpha_i^t \text{Re} p_t - \text{Im} \alpha_i^t \text{Im} p_t \right) \left( \sum_t \text{Re} \alpha_i^t \text{Re} p_t - \text{Im} \alpha_i^t \text{Im} p_t \right) = \hat{\sigma} \left( \sum_i \text{Re} \alpha_i^t \text{Re} p_t - \text{Im} \alpha_i^t \text{Im} p_t \right) \quad (33)$$

Therefore, it is essentially a one-hidden-layer fully connected network on  $\{(p_1, p_2)\} \simeq \mathbb{R}^4$ . Thus the set is dense.

Assume this is the case for  $n$ , and we would like to prove the lemma for  $n + 1$ . We denote  $2^n = N$ . Then the layer input has the following form:

$$\tilde{\sigma} \left( \sum_{t=0}^N a_i^t(p_0, \dots, p_{N/2}) p_t \right) \left( \sum_{t=0}^N a_i^t(p_0, \dots, p_{N/2}) g^t \right),$$

Now the new “ $a_i^t$ ” (denoted as  $b_i^t$ ) takes the following form:

$$b_i^t = \sum_{p+q=t} \sum_{j,k} \alpha_{ijk} \tilde{\sigma}(a_j^t p_t) \tilde{\sigma}(a_k^t p_t) a_j^p a_k^q.$$

Consider the bijection  $F : \mathbb{C}^{N+1} \rightarrow \mathbb{P}_N(\mathbb{C})$ , given by  $F(\vec{a}) = \sum_t a_t z^t$ . Using this we define

$$\vec{a} * \vec{b} = F^{-1}(F(\vec{a})F(\vec{b})).$$

Then

$$\vec{b}_i = \alpha_{ijk} \tilde{\sigma}(\vec{a}_j \cdot \vec{p}) \tilde{\sigma}(\vec{a}_k \cdot \vec{p}) \vec{a}_j \vec{a}_k = \alpha_{ijk} H(p, \vec{a}_j, \vec{a}_k).$$

This forms a linear space  $\mathcal{B}^{n+1} \subset (L^\infty(K_{n+1}))^{2N+1}$ . For simplicity we henceforth omit the subscript on  $K_{n+1}$ .

We assume  $(a_i^t)_{t=0}^N$  could approximate any constant function of  $p_1, \dots, p_{N/2}$ . This is trivially true when  $n = 1$ , since it is a function on a constant and takes arbitrary constant values.

Denoting  $e_0 = F^{-1}(1/d)$ , where  $d = \dim G$ , we have  $e_0 \cdot p = 1, \forall p \in K$ . Since  $K$  is compact, there exists an open set  $U$  s.t.  $e_0 \in \partial U$ , and  $b \cdot p \in (1, +\infty), \forall b \in U, p \in K$ .

On the other hand, it is easy to see that  $\{b * b : b = (1, z, \dots, z^N)\}$  is linearly independent as a subset. This way we could choose  $2N + 1$  elements  $\{b^{z^t}\}_{t=0}^{2N}$  from its intersection with  $U$ , such that  $\text{span}\{b^{z^t} * b^{z^t}\} = \mathbb{C}^{2N+1}$ .

Now given a constant vector  $\vec{b} = (b_0, \dots, b_{2N})$ , there exists  $\{\alpha_t\}$  such that  $\vec{b} = \alpha_t b^{z^t} * b^{z^t}$ . We want to show that  $\vec{b}$  can be approximated by any precision  $\epsilon$ .

Without loss of generality, assume  $\sup \tilde{\sigma} = 1$  and  $\inf \tilde{\sigma} = 0$ . Then, for all  $\epsilon$ , there exists  $M_0 > 0$  such that for all  $x > M_0/2$ ,  $\tilde{\sigma}(x) \in (\sqrt{1 - \epsilon}, 1)$ . This gives

$$\left| \frac{d^2}{M^2} H(p, M e_0, M e_0) - 1 \right| = |1 - \tilde{\sigma}(M)|^2 < \epsilon, \quad \forall M > M_0.$$

By induction, there exists  $a_t$  such that  $\|a_t - b^{z_t}\|_\infty < \min\{\epsilon, M/2\}$ . Consider

$$\vec{b}' = \alpha_t \frac{1}{M^2} H(p, a_t, a_t) = \alpha_t \tilde{\sigma}(M\alpha_t \cdot p)^2 a_t * a_t.$$

Then

$$\begin{aligned} |\vec{b}' - \vec{b}| &= |\alpha_t (\tilde{\sigma}(M\alpha_t \cdot p)^2 - 1) b^{z_t} * b^{z_t} + \tilde{\sigma}(M\alpha_t \cdot p) (b^{z_t} * b^{z_t} - \alpha_t * \alpha_t)| \\ &\leq \alpha_t \epsilon |b^{z_t} * b^{z_t}| + 2\epsilon |b^{z_t}| + \epsilon^2 \\ &\leq C(\vec{b}, N)\epsilon. \end{aligned} \tag{34}$$

When the coefficient functions approximate constants, the last layer is essentially a one-hidden-layer fully connected network over  $p_1, \dots, p_{2N}$ . Similar to the  $N = 1$  case, as the width grows larger the network can approximate any function  $f(p_1, \dots, p_{2N})$ . This concludes the proof of the lemma.  $\square$

We may now complete the proof of Theorem 7.

*Proof.* (Proof of Theorem 7)

Recall that by Theorem 2 the space of class functions  $L^2_{class}(G)$  is spanned by symmetric polynomials in the eigenvalues of group elements. Since these symmetric polynomials can be expressed in terms of traces  $\text{Tr}(g), \text{Tr}(g^n), \dots, \text{Tr}(g^M)$  it follows that any class function can be written as a function of these traces. Now, since  $G$  is compact, we have  $L^2(G) \supset L^\infty(G)$  and  $\|f\|_2 \geq C\|f\|_\infty$ . Therefore, for all  $f \in L^2_{class}(G)$ , and for any  $\epsilon > 0$ , there exists

$$f_n = f_n(p_1, \dots, p_n) \in L^\infty(K)$$

such that  $\|f - f_n\|_2 < 1/2\epsilon$ . By Lemma 8 the function class  $\mathcal{BLN}^k_{\tilde{\sigma}}(G)$ , consisting of neural networks with  $k$  gauge equivariant bilinear layers, can approximate any function  $f(p_1, \dots, p_k)$  arbitrarily well, provided  $k$  is large enough. We deduce that there exists  $g \in \mathcal{BLN}^n_{\tilde{\sigma}}(G) \subset L^\infty(G)$  such that  $\|g - f_n\|_\infty < 1/2C\epsilon$ . Therefore

$$\|g - f\|_2 < (C \cdot 1/2C + 1/2)\epsilon = \epsilon.$$

This concludes the proof of the main theorem.  $\square$

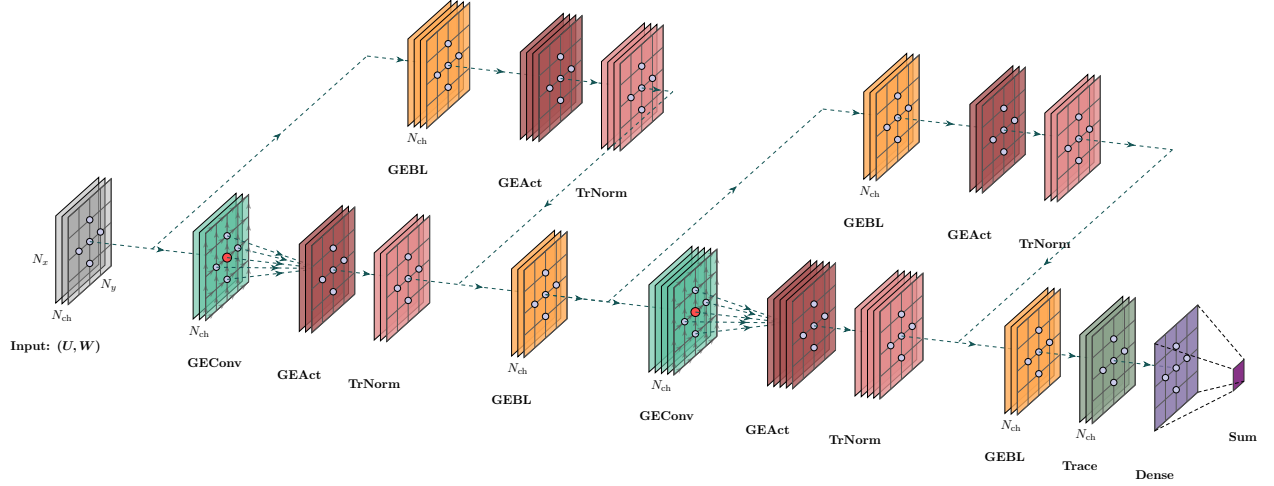


Figure 9: Architecture of GEConvNet. In this figure, the rectangles represent the spatial grid, the arrows on the grid represent links, and the number of layers ( $N_{ch}$ ) represents the number of channels ( $\gamma$ ). Each circle represents a site on the grid, and quantities on different sites do not interact with each other, except for the GEConv Layers, and the last summation on grids.

Table 4: Configuration of GEBL layers for the baseline model. See its architecture in Figure 2. In addition, every GEBL layer is followed by a GEAct layer and a TrNorm layer that maintains channel size.

Layer	Input Channel	Output Channel
GEBL 1	1	32
GEBL 2	32	16
GEBL 3	16	8

## D Further Details regarding the Network Structure

**Architecture of GEConvNet** Figure 10 is a demonstration of the architecture of GEConvNet. It has GEConv layers implemented inside, therefore takes the links  $U_k^\mu$  as inputs, beside the fluxes  $W_k$ , if the kernel size is set as positive.

**Configuration of the baseline model** Table 4 lists the hyperparameters for GEBL layers in the baseline model. Since the GEBL layers are consecutive with channel size-maintaining layers, GEAct and TrNorm layers in between, the former layer's output channel equals to the latter's input channel.

**Complexity-Accuracy Comparison** Figure 10 is a comparison of model complexity and accuracy across different models. All the models are all trained on a  $5 \times 5$  grid with 4 filled bands. Due to the instability of TrMLP, there are only 3 success runs with this model.

**Global Loss Curve for Training on Higher Order Chern Numbers** Figure 11 shows the global loss curve for training on second order Chern numbers. Since we adopt the  $L_1$ -norm  $\|\cdot\|_1$  here,  $L_g$  essentially measure the mean absolute error of global outputs.

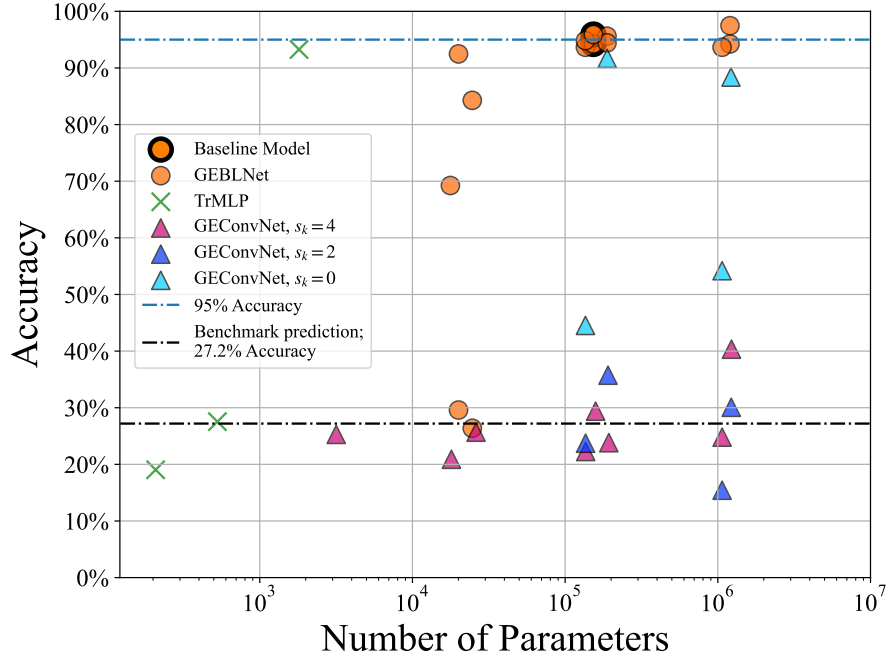


Figure 10: Comparison of model complexity and accuracy across different architectures. Complexity is measured by the number of learnable parameters, and  $s_k$  denotes the kernel size for GEConv layers. Each marker represents a training run with variations in models, learnable parameters, and random seeds.

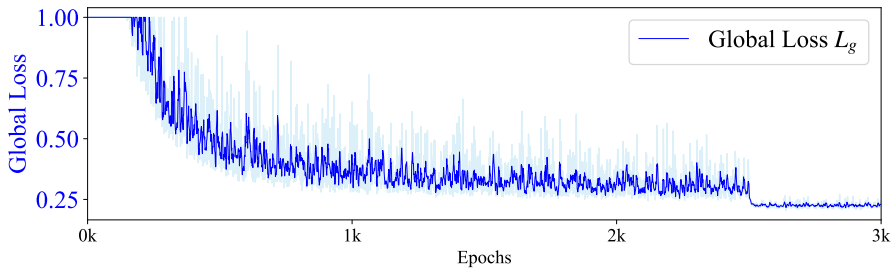


Figure 11: Global validation loss curve of the baseline model, trained on a  $3^4$  grid, with 3 filled bands to learn the second order Chern number  $\tilde{C}_2$ .